

Automated Polarized Hyperspectral Imaging (PHSI) for *ex-vivo* and *in-vivo* Tissue Assessment

Ling Ma ^{a,b}, Akhila Srinivas ^{a,b}, Abirami Krishnamurthy ^{a,b}, Ximing Zhou ^{a,b},
Nimit Subhashbhai Shah ^b, Girgis Obaid ^b, Baowei Fei ^{a,b,c,*}

^a Center for Imaging and Surgical Innovation, University of Texas at Dallas, Richardson, TX

^b Department of Bioengineering, University of Texas at Dallas, Richardson, TX

^c University of Texas Southwestern Medical Center, Department of Radiology, Dallas, TX

*Corresponding author: bfei@utdallas.edu, Website: <https://fei-lab.org>

ABSTRACT

Polarized light interactions with biological tissues can reveal information regarding tissue structure, while spectral characteristics are closely related to tissue composition. An integration of both modalities in a compact system could better assist tissue assessment. This study aims to develop a polarized hyperspectral imaging (PHSI) system that fulfills both linearly and circularly polarized hyperspectral imaging for *in vivo* and *ex vivo* applications. The system is comprised of a white LED, two linear polarizers, two liquid crystal variable retarders (LCVRs), and a hyperspectral snapshot camera. The system was calibrated to compute the full Stokes polarimetry. For tissue differentiation, fresh *ex vivo* mouse tissue specimens from kidney, liver, spleen, muscle, lung, and salivary gland of mice were imaged. The spectra of three features, named degree of polarization (DOP), degree of linear polarization (DOLP), and degree of circular polarization (DOCP), were generated. A k-nearest neighbor (k-NN) classifier was trained with multi-class spectra and 5-fold cross validation. It was found that DOP better differentiates tissue with an average accuracy of 0.87. Additionally, support vector machine (SVM) classifiers were trained to differentiate between each two of the organs, and it was determined that DOLP better identified kidney, liver, and spleen, whereas DOCP better identified muscle and lung tissues. Then, the setup was employed to image *in vivo* human fingers with and without a blood occlusion to qualitatively estimate oxygen saturation. Preliminary results demonstrate that both DOLP and DOCP reveal a distinction of oxygen saturation states. These results demonstrate the feasibility of the PHSI system for distinguishing between optical properties of tissues, which has the potential to reveal disease-related information for diverse medical applications.

Keywords: Polarized hyperspectral imaging, *ex vivo*, *in vivo*, tissue assessment, classification, oxygen saturation

1. INTRODUCTION

The rapid growth of medical techniques has brought up the need of fast, non-contact, and non-invasive tissue assessment. Hyperspectral imaging (HSI) and polarized light imaging (PLI) are two non-contact and label-free optical imaging modalities that have been emerging in recent years. HSI is famous for its ability to utilize both spatial and spectral information of the tissue and it is mostly implemented based on the diffuse reflected light ¹⁻⁶, while PLI is based on the scattered light and is specifically good for tissue structure analysis ⁷. Different tissues have different polarization properties, which helps differentiate tissue types or detect certain structures. Meanwhile, the intensity of scattered light is spectrally related to the size of scattering particles (molecules and cellular components), thus the diversity of scattering particles may result in unique spectral signatures of each polarization property. Combining spectroscopy with polarimetry may enrich the features that we can use for tissue assessment.

Although the randomness of tissue structures has a fast depolarization effect as the polarized light propagates in tissues, certain tissues or cell structures can preserve the degree of polarization detectable ⁷, making it a useful optical property for tissue analysis. In intensity-based polarimetry, Stokes vector is a commonly used representation of a light beam, which can be determined by four independent measurements, namely I_H , I_V , I_{45} , and I_{RC} (or I_{LC})⁸⁻¹⁰. The four elements are the light intensities measured with a horizontal linear analyzer, a vertical linear analyzer, a +45-degree oriented linear analyzer, and a right (or left) circular analyzer in front of the detector, respectively. From the Stokes vector, three features named

degree of polarization (DOP), degree of linear polarization (DOLP), and degree of circular polarization (DOCP) can be further derived.

There has been a long history of polarimetry studies in the biomedical field, such as the characterization of bacterial suspensions^{11,12}, measurement of cellular structures¹³, and the examination of clear tissues such as cornea and nerves^{14,15}. In recent years, polarized light imaging has been mainly investigated for the detection of skin cancer, especially melanoma¹⁶⁻¹⁹, as well as skin complications²⁰. However, in most studies, only the linear polarization characteristic of tissues was utilized, neglecting the circular polarized light from the tissues. In addition, some studies used manually rotated linear polarizers^{20,21} to acquire the co-polarized and cross-polarized light images separately. The manual operations might be inaccurate and increase the image acquisition time. In addition, studies have not been done to vastly investigate the polarization properties of various tissue types, which could potentially provide a new perspective for automatic tissue assessment.

In this paper, we developed an automated polarized hyperspectral imaging (PHSI) setup for multiple tissue assessment tasks. The compact system was able to automatically acquire full Stokes elements within 2 seconds without any rotating components. Linear and circular polarized light images from *ex vivo* mouse tissue samples and *in vivo* human hand were acquired, respectively. Three polarization features, namely DOP, DOLP, and DOCP of various tissue types were investigated and compared to validate the feasibility of using polarization properties for tissue assessments.

2. METHODS

2.1 Polarized hyperspectral imaging setup

The polarized hyperspectral imaging system comprised of two major parts, namely the illuminating branch and the imaging branch. The illuminating branch had a 15 mW white light-emitting diode (LED) light source and a linear polarizer (LP) to provide polarized illumination. The imaging branch consisted of two liquid crystal variable retarders (LCVRs), a linear polarizer, a 35 mm focal length convex lens, and a snapshot hyperspectral camera. All components were compactly assembled using cage plates and mounted vertically on an 8 inch \times 8 inch breadboard, with both branches targeting at the sample, as Figure 1(a) shows. The LED had a 25° half viewing angle which was sufficient to illuminate the field of view (FOV) of the camera, which was about 10 mm \times 10 mm. The snapshot camera had a 1088 \times 2048 pixels complementary metal-oxide-semiconductor (CMOS) imaging sensor with 4 \times 4 mosaic filters integrated on the sensor. The hypercubes acquired with the camera had a size of 270 pixels \times 510 pixels \times 16 bands covering the wavelength range of 460 nm ~ 600 nm.

The orientation of the linear polarizer and two LCVRs in the imaging branch are as shown in Figure 1(b). The fast axis of LCVR1 and the polarization axis of LP2 were both at 0 degree, while the fast axis of LCVR2 had a 45-degree angle with the x axis. In order to avoid strong glares in the I_H image, the polarization axis of LP1 in front of the LED light source was set at 45-degree orientation. By applying different voltages to the LCVRs, they could form different combinations of phase retardance, which changed the polarization status of the incoming light, so that the light might pass LP2 and be captured by the imaging sensor. The Jones matrices of LCVR1, LCVR2, and LP2 at different acquisition stages are listed under each component in Figure 1(b). Table 1 shows the phase retardance and the corresponding Jones Matrix of each LCVR for the acquisition of four Stokes vector elements, namely I_H , I_V , I_{45} , and I_{LC} . We implemented our own controlling software by incorporating the software development kits (SDKs) of the LCVR controller and the snapshot HSI camera, in order to automatically acquire all four Stokes vector elements. Each acquisition of all 4 images took less than 2 seconds. The low-heat illumination and the short image acquisition time could prevent tissue samples from being damaged and thus preserve their optical characteristics.

2.2 Image acquisition

In our study, the PHSI system was utilized to image both fresh *ex vivo* mouse tissue samples and *in vivo* human hand for different tasks, as shown in Figure 2. For the *ex vivo* tissues, each fresh sample was taken out from the buffer solution and immediately placed in a plate that was padded with dark-color paper towel and positioned at the center of the camera FOV. For the *in vivo* experiment, the hand was placed on the breadboard with the light source and imaging branch targeting at the region of interest on the hand. Then, different voltages were applied to the LCVRs, and the snapshot camera was synchronized to acquire a hyperspectral image at each of the 4 steps. For each sample, we acquired 4 images, namely I_H , I_V , I_{45} , and I_{LC} . The acquisition of entire 4 images of one sample took less than 2 seconds in total and was fully automatic.

After imaging all tissues, four white reference images were acquired separately for I_H , I_V , I_{45} , and I_{LC} , respectively. The white reference images and all tissue images were taken with the same illumination setting and the same camera integration time of 50 ms.

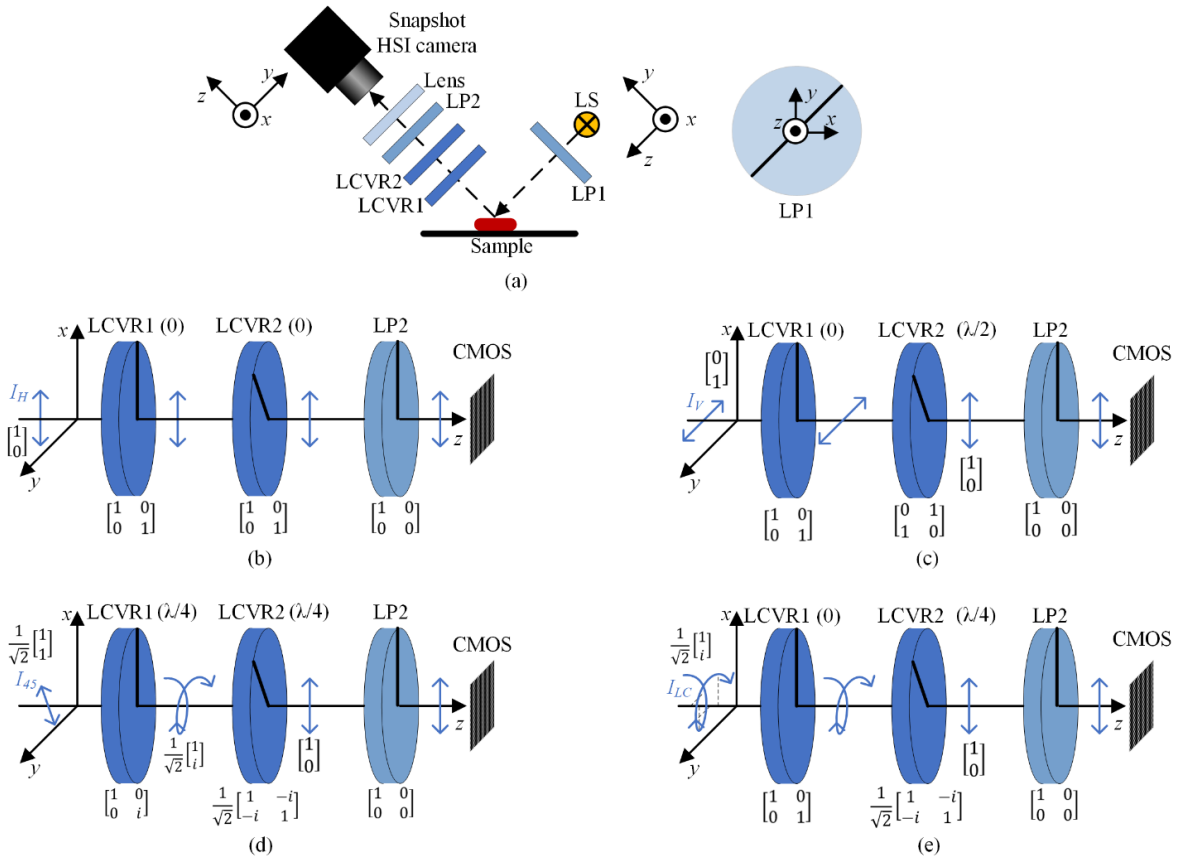
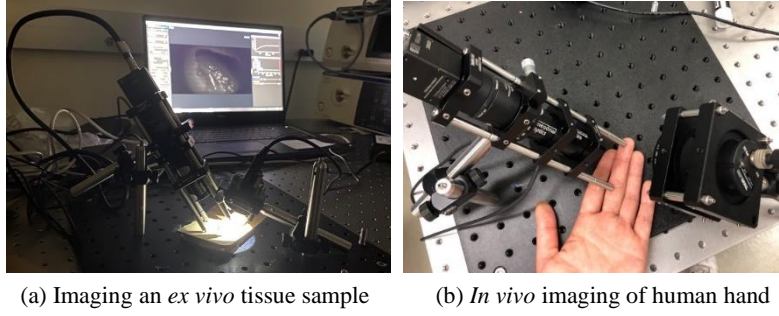


Figure 1. Illustration of the polarized hyperspectral imaging system and imaging mechanism. (a) Diagram of the imaging setup, comprising of an LED light source (LS), two linear polarizers (LP1 and LP2), two liquid crystal variable retarders (LCVR1 and LCVR2), and a snapshot hyperspectral camera. All components are placed parallel to the xy plane, and z is the direction of light propagation. The polarization axis of LP1 is 45 degrees to the x-axis. (b-e) Acquiring four Stokes vector elements, namely I_H , I_V , I_{45} , and I_{LC} , by changing the phases of two LCVRs. The solids lines indicate the fast axes of LVCRs and the polarization axis of LP2. Jones Matrices of the light and components are shown every time the polarization state of the light changes.

Table 1. Phase retardance and Jones matrices for the acquisition of 4 different Stokes element images.

Incoming polarized light	Phase retardance of LCVR1 (Fast axis at 0°)	Phase retardance of LCVR2 (Fast axis at 45°)
I_H $\begin{bmatrix} 1 \\ 0 \end{bmatrix}$	0 $\begin{bmatrix} 1 & 0 \\ 0 & 1 \end{bmatrix}$	0 $\begin{bmatrix} 1 & 0 \\ 0 & 1 \end{bmatrix}$
I_V $\begin{bmatrix} 0 \\ 1 \end{bmatrix}$	0 $\begin{bmatrix} 1 & 0 \\ 0 & 1 \end{bmatrix}$	$\lambda/2$ $\begin{bmatrix} 1 & 0 \\ 0 & -1 \end{bmatrix}$
I_{45} $\frac{1}{\sqrt{2}} \begin{bmatrix} 1 \\ 1 \end{bmatrix}$	$\lambda/4$ $\begin{bmatrix} 1 & 0 \\ 0 & i \end{bmatrix}$	$\lambda/4$ $\frac{1}{\sqrt{2}} \begin{bmatrix} 1 & 0 \\ 0 & i \end{bmatrix}$
I_{LC} $\frac{1}{\sqrt{2}} \begin{bmatrix} 1 \\ i \end{bmatrix}$	0 $\begin{bmatrix} 1 & 0 \\ 0 & 1 \end{bmatrix}$	$\lambda/4$ $\frac{1}{\sqrt{2}} \begin{bmatrix} 1 & 0 \\ 0 & i \end{bmatrix}$



(a) Imaging an *ex vivo* tissue sample (b) *In vivo* imaging of human hand

Figure 2. *Ex vivo* mouse tissue sample imaging for tissue differentiation as well as *in vivo* human hand imaging for oxygen saturation estimation using the PHSI system. Note that the ambient light was turned off during real image acquisition.

2.3 Data processing

After the image acquisition of each sample, we calibrated 4 hyperspectral images (I_H , I_V , I_{45} , and I_{LC}) with the corresponding white references²². Three bands (595 nm, 523 nm, and 461 nm) from each calibrated hypercube were extracted to form a pseudo-RGB image for better visualization. The location and size of glares in the images of the same sample may vary, although the images were taken under an identical illumination setting. Even if a pixel had glare in one image but no other three images, the spectral signature of this pixel would be inaccurate. Thus, glare removal was carried out for each single image before the calculation of Stokes parameters. Since the glare pixels were saturated, they tend to have much higher values than other pixels. Therefore, by summing all bands in a hypercube and applying a hard threshold, a mask of glares in this image can be easily generated. The masks of all four images were then combined together, so that the glare pixels from any one image would be excluded from all four images.

Then, full Stokes parameters were calculated using the calibrated images:

$$S_0 = I_H + I_V \quad (1)$$

$$S_1 = I_H - I_V \quad (2)$$

$$S_2 = I_{+45} \times 2 - S_0 \quad (3)$$

$$S_3 = S_0 - I_{LC} \times 2 \quad (4)$$

Based on the Stokes parameters, we calculated the degree of polarization, degree of linear polarization, and degree of circular polarization of each sample:

$$DOP = \sqrt{S_1^2 + S_2^2 + S_3^2} / S_0 \quad (5)$$

$$DOLP = \sqrt{S_1^2 + S_2^2} / S_0 \quad (6)$$

$$DOCP = \sqrt{S_3^2} / S_0 \quad (7)$$

The calculated DOP, DOLP, and DOCP had the same dimensions as the original hypercube. To intuitively show how much different tissues depolarize the light, we calculated the average DOP, DOLP, and DOCP across all 16 bands and generated heatmaps. Then, we extracted spectra of DOP, DOLP, and DOCP to quantitatively compare the polarization properties among different tissues. We observed the pseudo-RGB images, excluded the regions with glares or insufficient illumination, and extracted the spectral signatures of three polarization features using a sliding window. For the *ex vivo* tissues, we used a 9×9 sliding window with a step size of 5 pixels; while for the images of *in vivo* human hand, the window size was 19×19 due to the impact of fingerprints.

2.4 *Ex vivo* tissue differentiation

We firstly investigate the difference of polarization properties among tissues from various organs due to their diversity of chemical compositions and microstructures. An animal model of five mice was employed, and from each mouse we harvested 6 organs, namely the kidney, liver, spleen, lung, muscle, and salivary gland. The fresh tissues were kept in phosphate-buffered saline for preservation and were imaged within 20 minutes after the tissue collection.

To investigate the feasibility of tissue differentiation using polarization properties, we employed machine learning classifiers to classify spectra that were extracted from different organs. Firstly, an k-nearest neighbors (k-NN) classifier was implemented in Matlab 2021b for multi-class differentiation. Spectra of DOP, DOLP, and DOCP of all 6 organs were used to train and validate the model separately, and the overall accuracy of all 6 organs and the multi-class sensitivity of each organ were calculated as the evaluation metrics. Then, a binary support vector machine (SVM) model was trained to differentiate tissues between each pair of 2 organs, in order to further investigate if different tissues reveal certain dominant polarization properties. For the binary classification tasks, accuracy was calculated just to see how well two tissues can be differentiated. For both multiclass and binary classification models, we implemented 5-fold cross validation (CV). In each fold, one mouse was left out for testing, and data from 4 mice were used for training. The same data has not been used in both training and testing at the same time.

In both the multi-class and binary classification tasks, accuracy is the ratio of the number of correctly labeled spectra and the total number of spectra. In the multi-class classification, we calculated sensitivity for each class to measure how many spectra in each organ are correctly labeled.

$$Accuracy = \frac{\text{Number of correctly labeled spectra}}{\text{Total number of spectra}} \quad (8)$$

$$Sensitivity = \frac{TP}{TP+FN} \quad (9)$$

where TP and FN means true positive and false negative. For the sensitivity of one organ in the multi-class task, positive correspond to the organ, and negative correspond to all other 5 organs.

2.5 Qualitative *in vivo* oxygen saturation estimation

Oxygen saturation (sO₂) is an important index for tissue assessment and health monitoring. In this study, we investigate how sO₂ impact the polarization properties of tissue and validate the feasibility of sO₂ measurement based on degree of polarization.

We used the PHSI system to image a human finger before and after blood occlusion. First, the tip of a normal finger was imaged. Then, we put rubber band on the same finger for blood occlusion and acquired two set of images with 1minute intervals. Afterwards, the rubber band was removed, and another set of images was acquired of the finger during reperfusion. Finally, a set of 4 white reference images were obtained to calibrate the images. Full Stokes parameters as well as DOP, DOLP, and DOCP of the finger at 4 stages were calculated as shown in Eq (1-7).

3. RESULTS

3.1 *Ex vivo* tissue classification using polarization properties

We first compare overall preservation of light birefringence of different tissues. Figure 3 shows the pseudo-RGB images as well as the heatmaps of DOP, DOLP, and DOCP of six different organs from one mouse. Pseudo-RGB images were generated by extracting the 16th (595 nm), 8th (523 nm), and the 1st (461 nm) band from the processed hypercubes. For better visualization of the organs, the intensity of some pseudo-RGB images was increased, thus the background in those images seems brighter than others. The heatmaps were generated by calculating the average intensity across all 16 bands in a hypercube, in order to visually compare the polarization effect among different organs.

It is obvious that kidney, liver, and spleen generally have a stronger polarization effect than lung, salivary gland, and muscle. Among three polarization features, DOP is always the strongest since it measures the intensity of both linear polarized light and circular polarized light. Other than that, tissues typically have a better preservation of linear birefringence, resulting in a higher DOLP. Nevertheless, DOCP remains a detectable feature of tissues, especially for kidney, liver, and spleen. Note that some regions in the heatmaps reveal extremely high degree of polarization, which was

caused by the insufficient illumination. Because the light source and the camera located on the opposite side, the protruding shape of the tissue samples could result in shadows, which affected the calculated DOP, DOLP, and DOCP values, such as the top-left and bottom-left corners in the kidney and spleen images in Figure 3. Those regions were excluded when we extracted spectra and thus not used for the training and validation of machine learning classifiers.

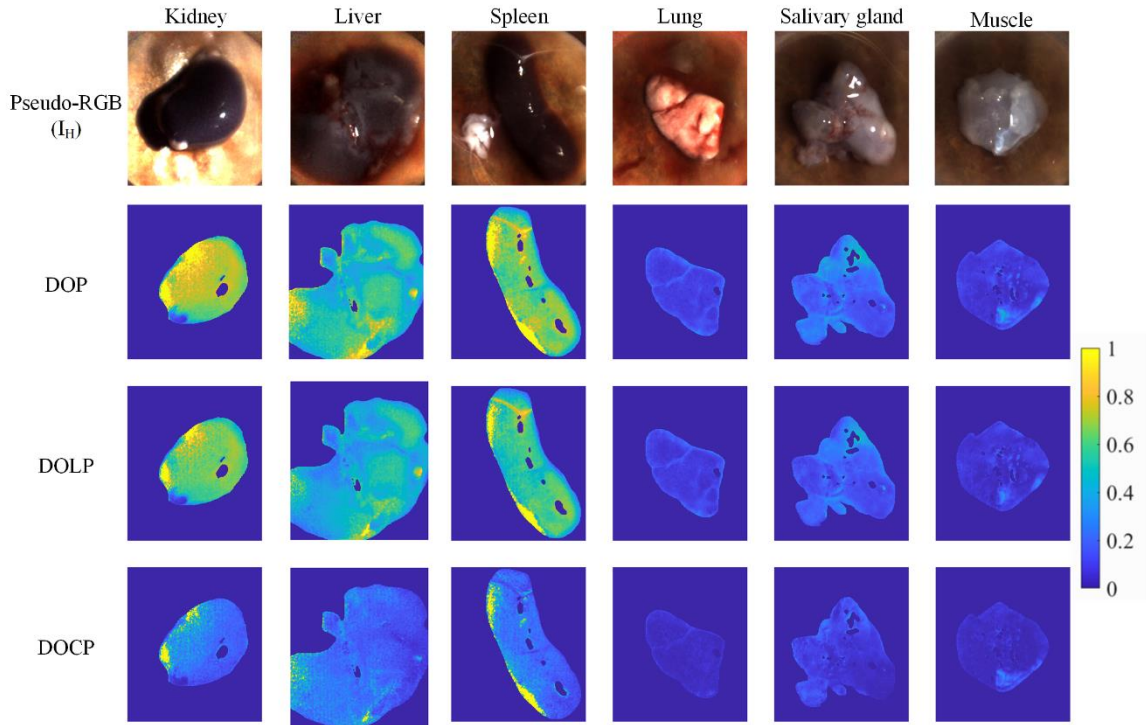


Figure 3. Pseudo-RGB images and heatmaps of DOP, DOLP, and DOCP of six different organs from one mouse. The pixel values of glare regions were set to zero in the heatmaps. All heatmaps were scaled in the range of 0~1.

In Figure 4, we compare the unnormalized spectral signatures of different organs from the same mouse. It can be seen that kidney, liver, and spleen have a better preservation of light birefringence compared to lung, salivary gland, and muscle. The tissues revealed a higher degree of linear polarization around 550 nm, while the degree of circular polarization was stronger before 500 nm.

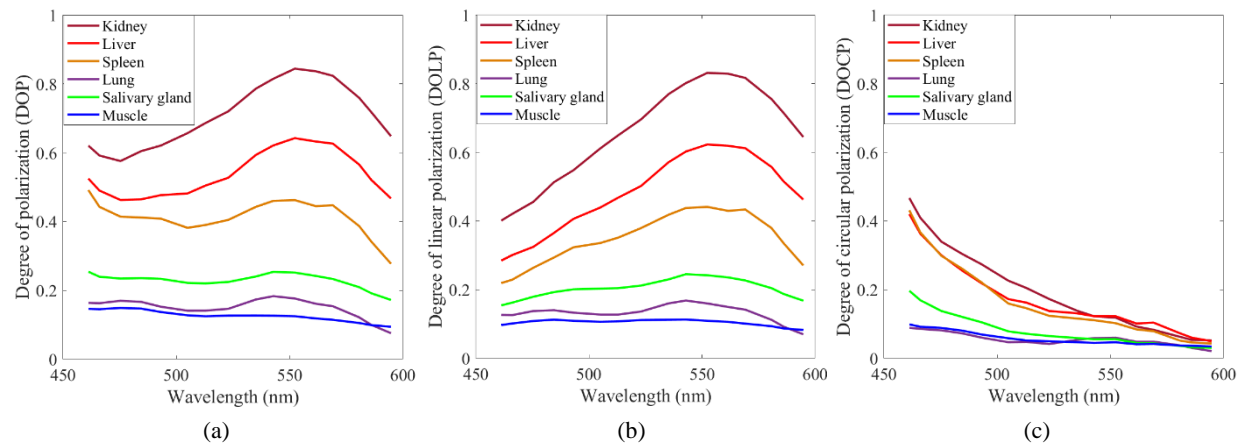


Figure 4. Comparison of DOP, DOLP, and DOCP of six organs from one mouse. (a) Average spectral signatures of DOP. (b) Average spectral signatures of DOLP. (c) Average spectral signatures of DOCP.

To further look into the spectral characteristics of DOP, DOLP, and DOCP, we normalize the spectra to eliminate the influence of spectra intensity. Each spectrum was divided by the sum of itself across all 16 bands. The mean and standard deviation of normalized spectral signatures of different tissues are shown in Figure 5. The spectra of kidney, liver, spleen, and salivary gland have a similar shape, while those of lung and muscle seem different. Except the strong DOLP peak at 550 nm that also exists in kidney, liver, spleen, and salivary gland, lung tissue has a good DOLP in the wavelength range of 460~500 nm. Muscle tissue, on the contrary, has relatively smooth and flat spectra of all three polarization features, not revealing a strong polarization character in any specific spectral band.

We trained a multi-class k-NN model for tissue differentiation. Five-fold cross validation was implemented, and the average classification accuracies of the cross validation using DOP, DOLP, and DOCP are shown in Table 2, where the overall accuracy of all spectra from six organs as well as multi-class sensitivity of each organ are given. It can be seen that DOP performed a generally better tissue differentiation, with an overall average accuracy of 0.87 and DOLP had a slightly lower overall performance. Specifically, kidney, liver, spleen, and salivary gland got obviously better results using DOP and DOLP compared to DOCP. Some kidney spectra (both DOP and DOLP) were classified as liver, which resulted in its low accuracy. This also happens in reflectance-based hyperspectral imaging, due to the similar color and texture of two organs. Regarding DOCP, it is interesting to find that lung and muscle, which had distinctive shapes of DOCP spectra, got fairly good classification performances compared to other four organs that shared a similar DOCP spectral shape. Despite that DOCP might not be sufficient enough as an individual feature for tissue classification, the results reveal that lung and muscle might have special circular polarization properties, which is worth more investigation.

Table 2. Average results of five-fold multiclass tissue differentiation.

Polarization feature	Multi-class sensitivity						Overall accuracy
	Kidney	Liver	Lung	Muscle	Salivary gland	Spleen	
DOP	0.67	0.93	0.92	0.78	0.79	0.89	0.87
DOLP	0.64	0.89	0.91	0.85	0.76	0.76	0.80
DOCP	0.21	0.66	0.89	0.79	0.60	0.55	0.62

After the multiclass tissue differentiation using data from all 6 organs, we further implemented binary classification between tissues from each pair of organs. Therefore, there were in total 15 tissue pairs, and for each pair we trained an SVM classifier with DOP, DOLP, and DOCP, respectively. Five-fold CV was implemented, and the average accuracy of all folds was calculated. Then, we compared the performance of DOP, DOLP, and DOCP, and report the polarization feature that resulted in the best tissue differentiation results, as shown in Table 3.

Despite that the multiclass tissue differentiation did not yield very high accuracy, mostly because of our small dataset volume, we did obtain very good binary classification results using the polarization properties of tissues. Generally, DOP and DOLP yielded significant good binary tissue differentiation with an accuracy above 0.90 in 12 tissue pairs. Especially, for those kidney, liver, and spleen, which had a similar tissue color, DOP and DOLP yielded fairly good differentiation. Kidney and liver still remain harder to separate compared to other tissue pairs, but the accuracy was improved to a large extent. Furthermore, DOCP had significant impact in classifications involving lung and muscle and generated better performance than DOP or DOLP. Even though DOP or DOLP had the best results for the “liver versus muscle” and “spleen versus lung” pairs, the classification performance using DOCP was very close. Thus, it proves that lung and muscle both have a distinctive DOCP property.

3.2 Qualitative oxygen saturation estimation

To validate the feasibility of oxygen saturation measurement using tissue polarization properties, we imaged the same finger before, during, and after blood occlusion. The average DOLP and DOCP spectral signatures of the finger at 4 different stages are shown in Figure 6 (a-b). There’s a general trend that the degree of linear polarization increases along with the deoxygenation of hemoglobin, while the degree of circular polarization decreases. We also generated the heatmap of DOP, DOLP, and DOCP of the fingertip based on their average values across all 16 wavelength bands, as shown in

Figure 6(c). The position of the finger in the images changed when we put on and removed the rubber band for blood occlusion, but we could still roughly locate the regions according to the fingerprint patterns. In Figure 6(c), black arrows indicate the same region in the finger where DOLP increased along with blood occlusion and decreased after reperfusion; red arrows indicate the region where DOCP decreased along with the blood occlusion and increased during reperfusion. Although the comparison was just qualitative, the results demonstrate an interesting trend of tissue, which provide us a promising perspective for future sO₂ measurement studies.

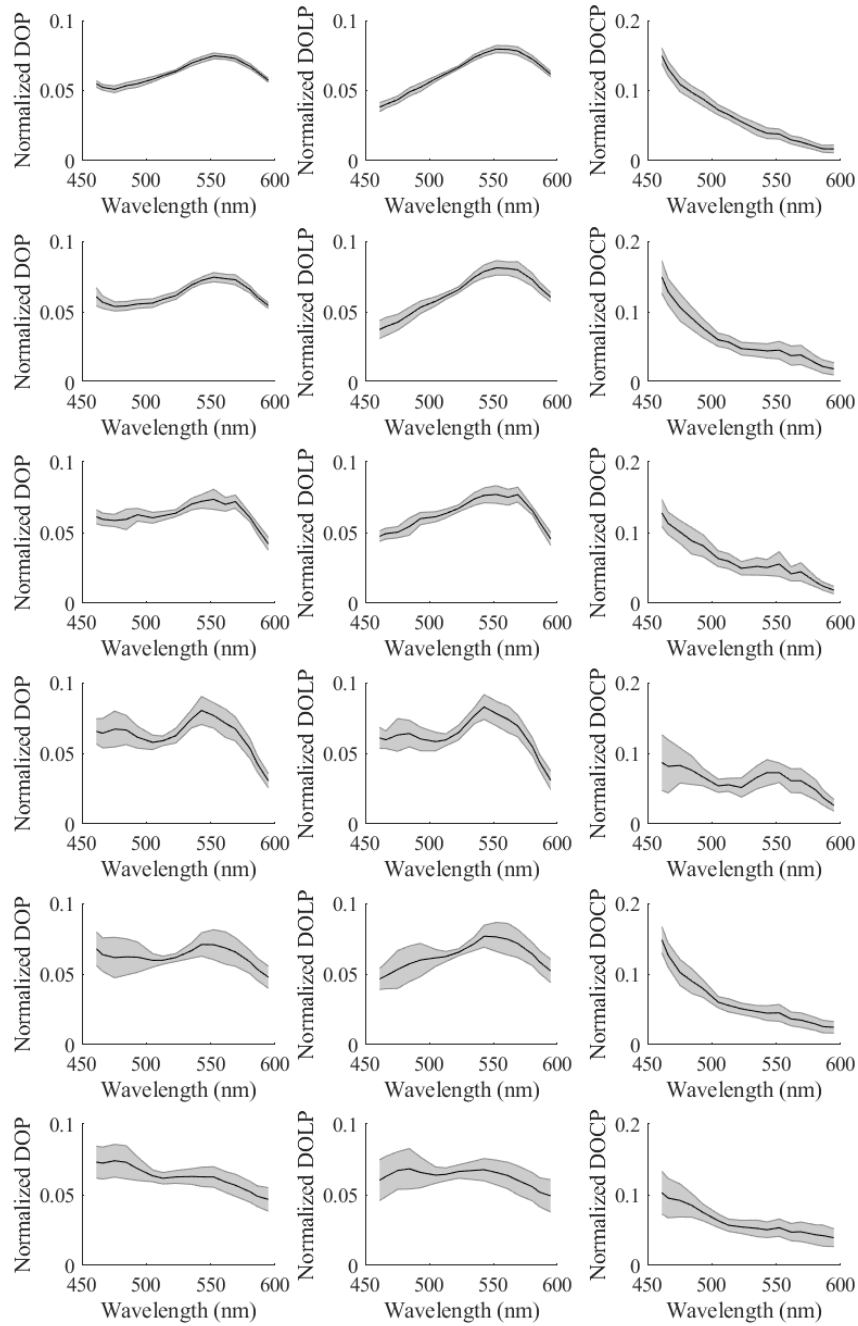


Figure 5. Normalized spectral signatures of DOP (left column), DOLP (middle column), and DOCP (right column) of 6 different organs from the mouse. From the top row to the bottom row: kidney, liver, spleen, lung, salivary gland, and muscle.

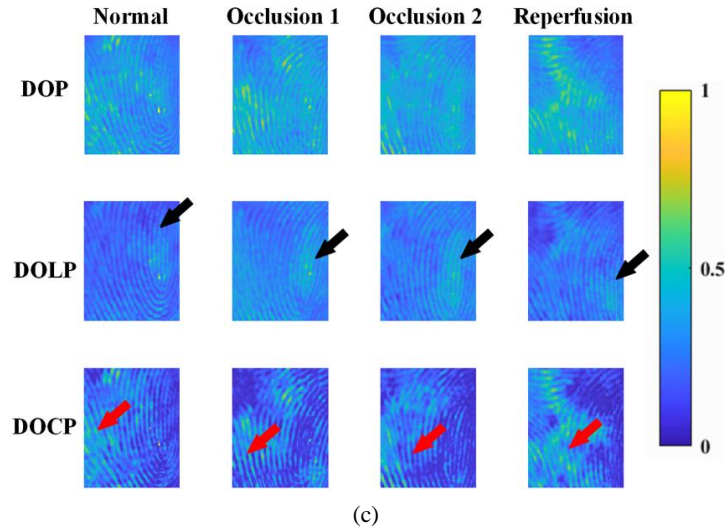
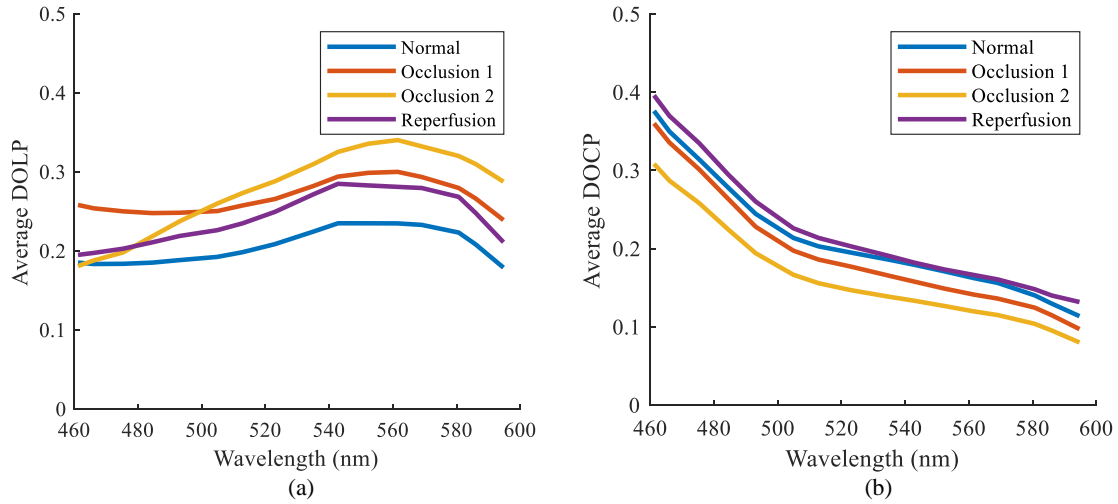


Figure 6. Change of DOP, DOLP, and DOCP along with the blood occlusion and the reperfusion of a finger. (a-b) Spectral signatures of DOLP and DOCP of a normal finger, finger with occlusions, and after reperfusion. (c) Heatmap of DOP, DOLP, and DOCP of a normal finger, finger with occlusions, and after reperfusion.

Table 3. Binary tissue classification results.

Organ 1	Organ 2	Best feature	Accuracy
Kidney	Liver	DOP	0.87
Kidney	Spleen	DOP	0.98
Kidney	Lung	DOP/DOLP	0.99
Kidney	Salivary gland	DOLP	0.99
Kidney	Muscle	DOLP	0.94
Liver	Spleen	DOP	0.91
Liver	Salivary gland	DOLP	0.99
Liver	Lung	DOP/DOLP/DOCP	0.99
Liver	Muscle	DOP	0.98
Spleen	Lung	DOP/DOLP	0.99
Spleen	Salivary gland	DOP/DOLP	0.99
Spleen	Muscle	DOP/DOLP	0.99
Lung	Salivary gland	DOP	0.94
Lung	Muscle	DOCP	0.85
Salivary gland	Muscle	DOCP	0.87

4. DISCUSSION & CONCLUSION

In this study, we developed a compact polarized hyperspectral imaging system, which was able to acquire images without any rotating part. The acquisition of a set of four images takes less than 2 seconds. We calculated full Stokes parameters, based on which we obtained the DOP, DOLP, and DOCP of the tissues for assessment. We firstly employed the system to image *ex vivo* fresh mouse tissues and implemented tissue differentiation. The results show that different tissues show distinctive polarization properties, which can facilitate the differentiation. Specifically, DOLP was the dominant polarization feature for kidney, liver, and spleen, while lung and muscle revealed distinctive DOCP spectral signatures. Then, we imaged an *in vivo* human finger to investigate the feasibility of oxygen saturation measurement using tissue polarization characteristics. The average spectra show that DOLP increases along with the blood occlusion while DOCP being the opposite. The qualitative comparison provided a new perspective for future sO₂ measurement studies.

However, our work had some limitations. Because of the low illumination intensity and the illuminating angle in our setup, some regions of the tissue samples were not well illuminated when the samples had a protruding shape, causing an inaccurate measurement of DOP in these regions. In addition, we had a relatively small amount of data from only 5 mice, and the glares in the images also reduced the amount of useful spectra. To address these two problems, we are planning to replace the single-LED light source with an LED ring illuminator, which will be able to provide a uniform and much brighter illumination. Thanks to the compact size (less than 160 mm length) and the light weight (less than 400 grams) of the imaging branch, we can possibly assemble the illuminating and imaging parts and make it a handheld device. We also plan to work on methods to eliminate glares during the image acquisition. With the portable device, we can hopefully acquire more data and further investigate the polarization properties of different types of tissue, as well as implementing quantitative analysis of oxygen saturation measurements.

In conclusion, the polarization characteristics of tissues contains rich information about tissue composition and microstructures, which can facilitate multiple tissue assessment and monitoring tasks such as tissue differentiation and oxygen saturation estimation. The compact polarized hyperspectral imaging device can many biological and medical applications.

ACKNOWLEDGMENTS

This research was supported in part by the U.S. National Institutes of Health (NIH) grants (R01CA156775, R01CA204254, R01HL140325, and R21CA231911) and by the Cancer Prevention and Research Institute of Texas (CPRIT) grant RP190588.

REFERENCES

1. G. Lu, and B. Fei, "Medical hyperspectral imaging: a review," *J Biomed Opt* **19**(1), 10901 (2014).
2. M. Halicek et al., "Hyperspectral imaging for head and neck cancer detection: specular glare and variance of the tumor margin in surgical specimens," *Journal of Medical Imaging* **6**(3), 035004 (2019).
3. M. Halicek et al., "In-Vivo and Ex-Vivo Tissue Analysis through Hyperspectral Imaging Techniques: Revealing the Invisible Features of Cancer," *Cancers* **11**(6), 756 (2019).
4. M. Halicek et al., "Hyperspectral Imaging of Head and Neck Squamous Cell Carcinoma for Cancer Margin Detection in Surgical Specimens from 102 Patients Using Deep Learning," *Cancers* **11**(9), 1367 (2019).
5. L. Ma et al., "Adaptive deep learning for head and neck cancer detection using hyperspectral imaging," *Visual Computing for Industry, Biomedicine, and Art* **2**(1), (2019).
6. M. Halicek et al., "Optical biopsy of head and neck cancer using hyperspectral imaging and convolutional neural networks," *J Biomed Opt* **24**(3), 1-9 (2019).
7. V. V. Tuchin, "Polarized light interaction with tissues," *J Biomed Opt* **21**(7), 071114 (2016).
8. X. Zhou et al., "Development of a new polarized hyperspectral imaging microscope," *Proc. SPIE 11213, Imaging, Therapeutics, and Advanced Technology in Head and Neck Surgery and Otolaryngology 2020*, 1121308 (2020).
9. X. Zhou, J. Dormer, and B. Fei, "Development of a polarized hyperspectral microscope for cardiac fiber orientation imaging," *Proc. SPIE 11215, Diagnostic and Therapeutic Applications of Light in Cardiology 2020*, 112150V (2020).

10. X. Zhou et al., "Automatic detection of head and neck squamous cell carcinoma on pathologic slides using polarized hyperspectral imaging and machine learning," *Proc. SPIE 11603, Medical Imaging 2021: Digital Pathology*, 116030Q (2021).
11. T. Bouvier et al., "Using light scatter signal to estimate bacterial biovolume by flow cytometry," *Cytometry* **44**(3), 188-194 (2001).
12. B. V. Bronk et al., "Measuring diameters of rod-shaped bacteria in vivo with polarized light scattering," *Biophysical Journal* **69**(3), 1170-1177 (1995).
13. V. Backman et al., "Polarized light scattering spectroscopy for quantitative measurement of epithelial cellular structures in situ," *IEEE Journal of Selected Topics in Quantum Electronics* **5**(4), 1019-1026 (1999).
14. R. W. Hart, and R. A. Farrell, "Light Scattering in the Cornea," *J. Opt. Soc. Am.* **59**(6), 766-774 (1969).
15. X.-R. Huang, and R. Knighton, "Linear birefringence of the retinal nerve fiber layer measured in vitro with a manuscript imaging micropolarimeter running head: birefringence of RNFL," *J Biomed Opt* **7**(2), (2002).
16. A. N. Yaroslavsky, V. Neel, and R. R. Anderson, "Fluorescence polarization imaging for delineating nonmelanoma skin cancers," *Optics Letters* **29**(17), 2010-2012 (2004).
17. E. Salomatina-Motts, V. A. Neel, and A. N. Yaroslavskaya, "Multimodal polarization system for imaging skin cancer," *Optics and Spectroscopy* **107**(6), 884-890 (2009).
18. D. Louie et al., "Degree of optical polarization as a tool for detecting melanoma: proof of principle," *J Biomed Opt* **23**(12), 125004 (2018).
19. A. N. Yaroslavsky et al., "Dual-Wavelength Optical Polarization Imaging for Detecting Skin Cancer Margins," *Journal of Investigative Dermatology* **140**(10), 1994-2000.e1991 (2020).
20. V. Dremin et al., "Skin Complications of Diabetes Mellitus Revealed by Polarized Hyperspectral Imaging and Machine Learning," *IEEE Transactions on Medical Imaging* **40**(4), 1207-1216 (2021).
21. C. He et al., "Characterizing microstructures of cancerous tissues using multispectral transformed Mueller matrix polarization parameters," *Biomed. Opt. Express* **6**(8), 2934-2945 (2015).
22. L. Ma, M. Halicek, and B. Fei, "In vivo cancer detection in animal model using hyperspectral image classification with wavelet feature extraction", *Proc. SPIE 11317, Medical Imaging 2020: Biomedical Applications in Molecular, Structural, and Functional Imaging*, 113171C (2020).